Applied Mathematics and Computation 237 (2014) 120–132

Contents lists available at ScienceDirect

Applied Mathematics and Computation

journal homepage: www.elsevier.com/locate/amc

An approximate method for Abel inversion using Chebyshev polynomials

Rajesh K. Pandey [a,*], Suraj Suman [a], Koushlendra K. Singh [a], Om P. Singh [b]

[a] PDPM Indian Institute of Information Technology, Design & Manufacturing Jabalpur, MP 482005, India
[b] Department of Mathematical Sciences, Indian Institute of Technology, Banaras Hindu University, Varanasi 221005, India

ARTICLE INFO

Keywords:
Abel inversion
Chebyshev polynomials
Operational matrix
Noise resistance

ABSTRACT

Many problems in physics like reconstruction of the radially distributed emissivity from the line-of-sight projected intensity, the 3-D image reconstruction from cone-beam projections in computerized tomography, etc. lead naturally, in the case of radial symmetry, to the study of Abel's type integral equation. In this paper, a new stable algorithm based on shifted Chebyshev polynomial approximation is presented and analyzed. First, Chebyshev operational matrix of integration P is constructed and then it is used to reduce the integral equation to a system of algebraic equation which can be solved easily. The method is quite accurate and stable even though the approximations are performed using polynomials of degree up to 5. Some test examples from the plasma diagnostics are illustrated to demonstrate the effectiveness and stability of the proposed method.

1. Introduction

Abel's integral equation [1] occurs in many areas of physics and engineering such as plasma diagnostics, astronomy, geophysics and image analysis. Usually, physical quantities accessible to measurement are quite often related to physically important but experimentally inaccessible ones by Abel's integral equation. Some of the studies where Abel's integral equation is widely applicable are: seismology [2], satellite photometry of airglows [3], electron emission [4], atomic scattering [5], flame and plasma diagnostics [6], and X-ray radiography [7].

In flame and plasma diagnostics the Abel's integral equation relates the emission coefficient distribution function of optically thin cylindrically symmetric extended radiation source (particularly a plasma source) to the line-of-sight radiance measured in the laboratory. To obtain the physically relevant quantity from the measured one requires the inversion of the Abel's integral equation, and in case the object does not have radial symmetry, it requires, in principle, the inversion of Radon transform [8].

The relation between the radial distribution of the emission coefficient $\varepsilon(r)$ and measured intensity $I(y)$ from outside of the source is described by the Abel transform. The Abel transform can be interpreted as the projection of a circularly symmetric function along a set of parallel lines of sight which are at distance y from the origin (referring to the Fig. 1). Reconstruction of the emission coefficient from its projection is known as Abel inversion.

For a cylindrically symmetric, optically thin, extended radiation source the relationship between the emissivity $\varepsilon_\lambda(r)$ and the intensity $I_\lambda(y)$, as measured from outside the source is given as [9],

* Corresponding author.
E-mail addresses: rkpandey@iiitdmj.ac.in, wavelet_r@yahoo.co.in (R.K. Pandey).

http://dx.doi.org/10.1016/j.amc.2014.03.043
0096-3003/

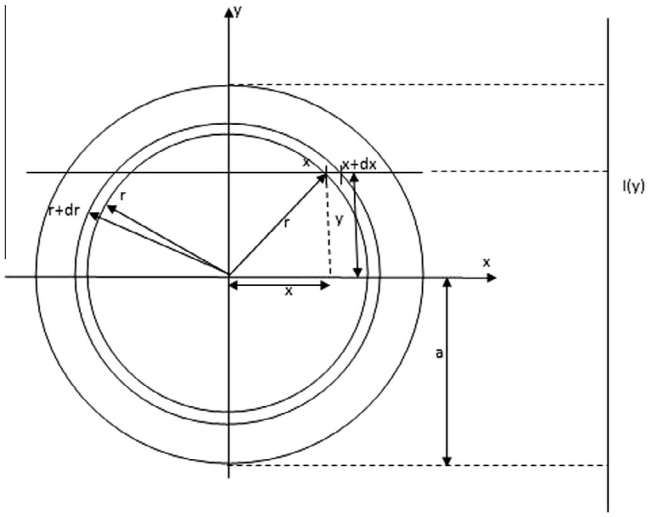

Fig. 1. Geometrical interpretation of the Abel transform in two dimensions with radius a.

$$I_\lambda(y) = \int_{-\sqrt{a^2-y^2}}^{\sqrt{a^2-y^2}} \varepsilon_\lambda(r)\, dr \tag{1}$$

for a particular wavelength λ, where y is the displacement of the intensity profile from the plasma centerline, r is the radial distance from the center of the source $x^2 + y^2 = r^2$, and a is the source radius. It is assumed that $\varepsilon_\lambda(r)$ vanishes for $r > a$, and hence $I_\lambda(y)$ vanishes for $|y| > a$. For simplicity, we take $a = 1.0$ in Eq. (1). Placing the variable of integration to r in Eq. (1), we obtain

$$I(y) = 2\int_y^1 \frac{\varepsilon(r) r}{\sqrt{r^2 - y^2}}\, dr, \quad 0 \leqslant y \leqslant 1, \tag{2}$$

a special form of Abel's integral equation, where we have dropped the suffix λ from $I_\lambda(y)$ and $\varepsilon_\lambda(r)$.

The analytical inversion of Eq. (2) is given as [10],

$$\varepsilon(r) = -\frac{1}{\pi}\int_r^1 \frac{1}{\sqrt{y^2 - r^2}} \frac{dI(y)}{d(y)} dy, \quad 0 \leqslant r \leqslant 1. \tag{3}$$

If the data function (projected intensity $I(y)$) is given approximately only at a discrete set of data points then the process of estimation of the solution function (emissivity $\varepsilon(r)$) becomes ill-posed because presence of small errors in the data $I(y)$ might cause large errors in the reconstructed solution. This is due to the fact that these formulae require differentiation of the measured data. In fact, two explicit analytic inversion formulae were given by Abel [1], but their direct application amplifies the experimental noise inherent in the radiance data significantly [11]. In 1982, a third analytic but derivative free inversion formula was obtained by Deutsch and Beniaminy [12] to avoid this problem.

In addition, some more numerical inversion methods [12–19] have been developed and each of these methods has some limitation depending upon the presence of error in the measured data. In 1992, Mejia et al. [20] have analyzed the stable Abel inversion through measured data on a discrete set of points using piecewise constant and piecewise linear interpolation techniques. Later, some new developments on Abel inversion have also been presented by many researchers such as Cho and Na [21], and George Chan and Hieftjen [22].

As per author's knowledge, the latest contributions on Abel's inversions are summarized as follows. In 2006, Yousefi [23] has provided Legendre wavelet based method for solving Abel integral equations. In [24], Pandey et al. have discussed analytical methods like Homotopy perturbation method (HPM), modified Homotopy perturbation method (MHPM), Adomian decomposition method (ADM) and modified Adomian decomposition method (MADM) for solving Abel integral equations. Further, Singh et al. [25], presented a stable algorithm for Abel's inversion using Bernstein's polynomials. Ma et al. [26–27], have presented Legendre polynomials and Legendre wavelets based stable algorithms for Abel's inversion. Li et al. [28], have provided and analyzed an efficient and stable method for Abel's inversion using generalized Taylor–Stieltjes polynomial approximation. Further, Huang et al. [29] discussed an approximate method for solving Abel integral equation by approximating the unknown function using Taylor series. In [30], Singh et al. constructed an operational matrix of integration based on orthonormal Bernstein polynomials, and used it to propose an algorithm for solving the Abel's integral equation. They have also studied the stability of the method under the effect of fixed noise. Consequently, the direct use of Eq. (3) is restricted and stable numerical methods are important.

The aim of this paper is to present and analyze a new stable algorithm for the numerical solution of Abel's integral Eq. (2) based on the constructed Chebyshev operational matrix of integration. The constructed Chebyshev operational matrix reduces Eq. (2) to a system of algebraic equations. By solving the system of algebraic equations, the inversion of Abel's integral equation is easily obtained. The presented method has also been tested with effect of noise in the input function. Some test examples from the plasma diagnostics having analytical inversions are considered to demonstrate the effectiveness and stability of the proposed method.

2. Chebyshev polynomials

The Chebyshev polynomials of first kind with orthogonality property in interval $[-1,1]$ are defined as follows:

$$S_{n+1}(x) = 2xS_n(x) - S_{n-1}(x), \tag{4}$$

where, $S_0(x) = 1$ and $S_1(x) = x$.

The orthogonality property of Chebyshev polynomials is given as:

$$\int_{-1}^{1} S_m(x)S_n(x)w(x)dx = \begin{cases} 0 & \text{if } m \neq n \\ \pi & \text{if } m = n = 0 \\ \frac{\pi}{2} & \text{if } m = n \neq 0 \end{cases},$$

where, $w(x) = 1/\sqrt{1-x^2}$ is the weight function. In order to convert the whole analysis in the interval $[0,1]$, we replace x by $(2x-1)$ in the Chebyshev polynomial recurrence relation as defined in Eq. (4)

$$c_{n+1}(x) = S_{n+1}(2x-1),$$

where, $c_n(x)$ are the shifted Chebyshev orthonormal polynomials in the interval $[0,1]$ with weight $w(x) = 1/\sqrt{1-(2x-1)^2}$. We call them orthonormal shifted Chebyshev polynomials and denote them as $c_0(x), c_1(x), c_2(x), \ldots, c_n(x)$. The orthonormal property of shifted Chebyshev polynomials is given as:

$$\int_0^1 c_i(x)c_j(x)w(x) = \begin{cases} 0 & \text{if } i \neq j \\ 1 & \text{if } i = j \end{cases}.$$

3. Outline of the method

A function $f \in L^2[0,1]$ may be approximated in terms of the shifted Chebyshev polynomials as:

$$f(r) = \lim_{n\to\infty} \sum_{i=0}^{n} a_i c_i(r), \tag{5}$$

where, $a_i = \langle f, c_i \rangle_w$ and $\langle , \rangle_w$ is the standard inner product on $L^2[0,1]$ with respect to weight $w(1) = 1/\sqrt{1-(2r-1)^2}$.

If the series given by Eq. (5), is truncated at $n = m$, then we have

$$f(r) \cong \sum_{i=0}^{m} a_i c_i(r) = F^T C(r), \tag{6}$$

where, F and $C(r)$ are matrices of order $(m+1)\times 1$, given by

$$F = [a_0, a_1, \ldots, a_m]^T \tag{7}$$

and

$$C(r) = [c_0(r), c_1(r), \ldots, c_m(r)]^T. \tag{8}$$

The elements of the matrix $C(r)$ are the shifted Chebyshev polynomials which are orthonormal in the interval $[0,1]$ with respect to the weight $w(r) = 1/\sqrt{1-(2r-1)^2}$ By change of variables, the Eq. (2) reduces to

$$I(\sqrt{y}) = \int_y^1 \frac{\varepsilon(\sqrt{r})}{\sqrt{r-y}}\, dr, \quad 0 \leqslant y \leqslant 1,$$

which takes the form,

$$I_1(y) = \int_y^1 \frac{\eta(r)}{\sqrt{r-y}}\, dr, \text{ where } I_1(y) = I(\sqrt{y}) \quad \text{and} \quad \eta(r) = \varepsilon(\sqrt{r}). \tag{9}$$

Using Eq. (6), the projected intensity $I_1(y)$ and emissivity $\eta(r)$ are approximated as

$$\eta(r) = A^T C(r) \tag{10}$$

and

$$I_1(y) = F^T C(y), \tag{11}$$

where the matrix F is known. From Eqs. (9)–(11), we obtain

$$F^T C(y) = \int_y^1 \frac{A^T C(r)}{\sqrt{r-y}} dr. \tag{12}$$

The right hand side of Eq. (12) involves evaluating the integrals of the types

$$\phi_n = \int_y^1 \frac{r^n}{\sqrt{r-y}} dr, \quad \text{for } n = 0, 1, \ldots, m,$$

where

$$\phi_0 = 2\sqrt{1-y} \quad \text{and} \quad \phi_n = \frac{1}{2n+1}(\phi_0 + 2ny\phi_{n-1}). \tag{13}$$

From Eq. (8), (12), and (13), it follows that

$$\int_y^1 \frac{C(r)}{\sqrt{r-y}} dr = PC(y), \tag{14}$$

where P is a square matrix of order $(m+1)\times(m+1)$. The matrix P is called the operational matrix of integration of the Chebyshev polynomials, named as Modified Chebyshev operational matrix of integration. The elements of the matrix P are calculated using the following formula, $P_{i,j} = \int_0^1 [c_j(y)w(y)(\int_y^1 \frac{c_i(t)}{\sqrt{t-y}} dt)]dy$. For $m = 5$, the modified Chebyshev operational matrix of integration P for the Eq. (14), can be obtained as

$$\mathrm{P} = \begin{pmatrix} 1.273 & -0.6 & -0.12 & -0.051 & -0.029 & -0.018 \\ 0.2 & 0.509 & -0.364 & -0.094 & -0.046 & -0.028 \\ -0.504 & 0.445 & 0.434 & -0.284 & -0.074 & -0.037 \\ -0.061 & -0.215 & 0.342 & 0.37 & -0.244 & -0.063 \\ -0.134 & 0.025 & -0.133 & 0.285 & 0.326 & -0.217 \\ -0.031 & -0.079 & 0.033 & -0.1 & 0.248 & 0.295 \end{pmatrix}.$$

Substituting Eq. (13) in Eq. (12), one obtains

$$A^T = F^T P^{-1}. \tag{15}$$

Hence, the approximate solutions $\eta(r)(= \varepsilon(\sqrt{r}))$ for the Abel's integral equation (2) are obtained by putting the values of A^T from Eq. (15) in Eq. (10).

4. Results and discussions

In this section, we discuss the implementation of our proposed algorithm and investigate its accuracy and stability by applying it on test functions with known analytical Abel inversions. It is always desirable to test a numerical inversion method using simulated data for which the analytical results are known and thus a comparison between the inverted results and the analytical results are possible. Here, five well known test profiles of different nature are considered for the purpose. Test examples 1, 2 and 3 have Gaussian profiles with $\eta(1) = 0$, and are commonly used in the literature. However, test example 4 is different and their inversions are evaluated using the complimentary Abel's integral equation,

$$I(y) = 2\int_0^y \frac{\varepsilon(r)r}{\sqrt{y^2-r^2}} dr. \tag{16}$$

For this study, a different operational matrix of integration Q is constructed to invert the test examples 4 and 5. The elements of the matrix Q are calculated using the following formula, $Q_{i,j} = \int_0^1 [c_j(y)w(y)(\int_0^y \frac{c_i(t)}{\sqrt{y-t}} dt)]dy$. The operational matrix of integration Q obtained corresponding to Eq. (15) is given as follows:

$$Q = \begin{pmatrix} 1.273 & 0.6 & -0.12 & 0.051 & -0.029 & 0.018 \\ -0.2 & 0.509 & 0.364 & -0.094 & 0.046 & -0.028 \\ -0.504 & -0.445 & 0.434 & 0.284 & -0.074 & 0.037 \\ 0.061 & -0.215 & -0.342 & 0.37 & 0.244 & -0.063 \\ -0.134 & -0.025 & -0.133 & -0.285 & 0.326 & 0.217 \\ 0.031 & -0.079 & -0.033 & -0.1 & -0.248 & 0.295 \end{pmatrix}.$$

The accuracy of the proposed method is demonstrated by calculating the parameters of absolute error $\Delta\eta(r_i)$ and average deviation σ which is also known as root mean square(RMS) error. They are calculated using the following equations:

$$\Delta\eta(r_i) = |\eta_a(r_i) - \eta_c(r_i)| \tag{17}$$

and

$$\sigma = \left\{\frac{1}{N}\sum_{i=1}^{N}[\eta_a(r_i) - \eta_c(r_i)^2]\right\}^{1/2} = \left\{\frac{1}{N}\sum_{i=1}^{N}\Delta\eta^2(r_i)\right\}^{1/2} = ||\Delta||_{2''}, \tag{18}$$

where, $\eta_c(r_i)$ is the emission coefficient calculated at point r_i, and $\eta_a(r_i)$ is the exact analytical emissivity at the corresponding point. Note that σ is the discrete l^2-norm of the absolute error $\Delta\eta$, which is denoted by $\|\Delta\eta\|_{2''}$. We also compute the continuous L^2-norm of the error $\Delta\eta$ using the following formula:

$$\|\Delta\eta\|_2 = \left[\int_0^1 \Delta\eta^2(r)\,dr\right]^{1/2}. \tag{19}$$

In all the test examples, the exact data function is denoted by $I_1(y)$, and the noisy data function $I_1^\delta(y)$ is obtained by adding a δ times random error to $I_1(y)$ such that, $I_1^\delta(y) = I_1(y) + \delta\theta$, where, δ is a small constant and θ is the uniform random variable with values in $[-1,1]$. Similar procedure is followed for noise analysis to the emissivity profiles and hence the matrices A and F, as stated in Eqs. (10) and (11), under the effect of noises, are obtained. For analyzing the errors under effect of random noise with number of sample points (N), the noisy data $I_1^\delta(y)$ are obtained such that, $I_1^\delta(y_i) = I_1(y_i) + \delta\theta_i$, where, $y_i = ih$, with the step size (h), $i = 1,\ldots,N, Nh = 1$ and θ_i is the uniform random variable with values in $[-1,1]$ such that $\underset{1\leqslant i\leqslant N}{Max}|I_1^\delta(y_i) - I_1(y_i)| \leqslant \delta$

The following examples are solved with and without random noise to illustrate the efficiency and stability of the proposed method by choosing three different values of the random noises δ_j as $\delta_0 = 0$, $\delta_1 = \sigma$ and $\delta_2 = p\%$ of μ, where $\mu = \frac{1}{N}\sum_{i=1}^{N} I_1(y_i)$, and hence the associated respective errors $Ej(r)$ for $j = 0,1,2$ are obtained.

Each of the test examples are analyzed and obtained results are plotted in the different figures. These figures represent the comparison between

(i) intensity profiles $I1(y)$ $(=I_1(y))$ and $I2(y)$ $(=I_1^{\delta_2}(y))$.
(ii) emissivity profiles $\eta(r)$, $\eta1(r)$ $(=\eta_{c_0}(r))$, $\eta2(r)$ $(=\eta_{c_1}(r))$ and $\eta3(r)$ $(=\eta_{c_2}(r))$.
(iii) the associated errors $\Delta\eta_{c_0}$, $\Delta\eta_{c_1}$ and $\Delta\eta_{c_2}$, respectively.

Figs. 2, 7 and 10 show the intensity profile $I1(y)$ $(=I_1(y))$ and $I2(y)$ $(=I_1^{\delta_2}(y))$. Figs. 3, 8, 11, 13 and 17 compare the exact solution $\eta(r)$ with the three computed solutions $\eta0(r)$ (without noise), $\eta1(r)$ (with random noise $\delta_1\theta_i$) and $\eta2(r)$ (with random noise $\delta_2\theta_i$), and Figs. 4, 9, 12 and 14 show the errors $E0(r)$ $(=\Delta\eta_{c_0}$: without noise), $E1(r)$ $(=\Delta\eta_{c_1}$: with random noise $\sigma\theta_i)$ and $E2(r)$ $(=\Delta\eta_{c_2}$: with random noise $\delta_2\theta_i)$ for illustrated test examples. The comparison of the absolute errors (with noise δ_1 and δ_2) on the different number of sample points(N) are shown in Figs. 5, 6, 15, 16 and 18.

Test example 1. We take the pair [21,22,28]

$$\eta(r) = \frac{1}{2}(1 + 10r - 23r^2 + 12r^3), \quad 0 \leqslant r \leqslant 1,$$

$$I_1(y) = \frac{8}{105}(19 + 34y - 125y^2 + 72y^3)\left(\sqrt{1-y}\right), \quad 0 \leqslant y \leqslant 1.$$

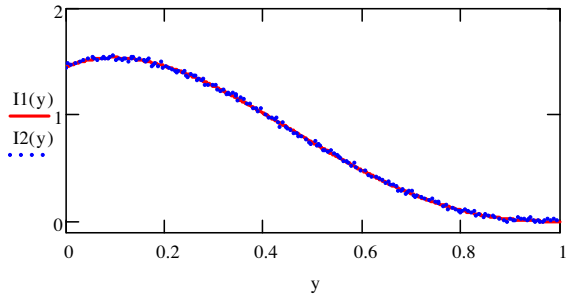

Fig. 2. Distributions of the lateral intensity in test example 1, without noise (I1(y)) and with noise (I2(y)).

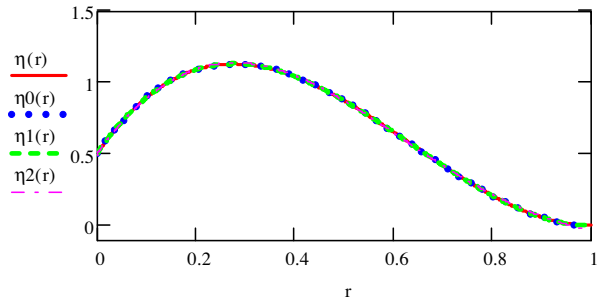

Fig. 3. Reconstructed inverse Abel transforms (emissivity) for test example 1 where profiles are presented as exact profile ($\eta(r)$), approximated profile without noise ($\eta^0(r)$), approximated profile with noise $\delta_1(\eta 1(r))$, and approximated profile with noise δ_2 ($\eta 2(r)$).

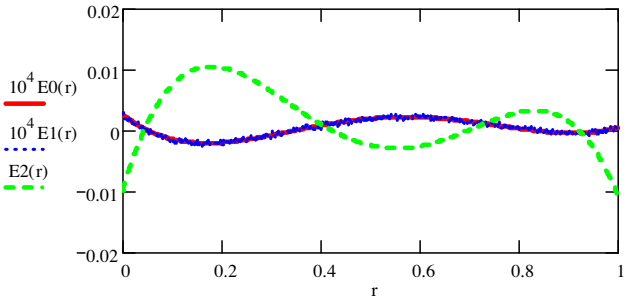

Fig. 4. Comparison of the errors for test example 1, where E0(r) represents error without noise, E1(r) error with noise δ_1, and E2(r) represents error with noise δ_2.

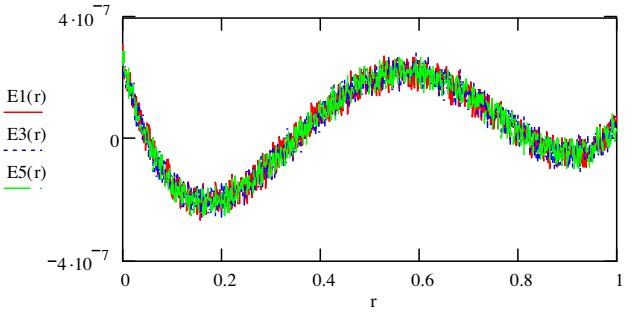

Fig. 5. Comparison of the errors with noise δ_1 for $N = 1000$ (E1(r)), $N = 500$ (E3(r)) and $N = 100$ (E5(r)) for test example 1.

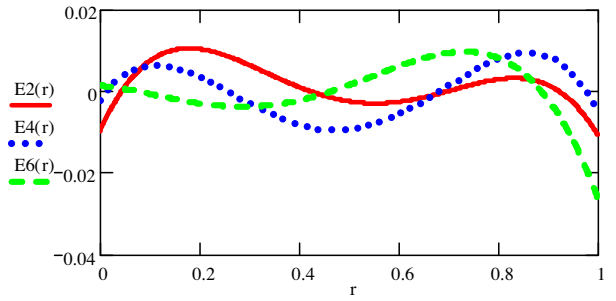

Fig. 6. Plot of errors with noise δ_2 for $N = 1000$ (E2(r)), $N = 500$ (E4(r)) and $N = 100$ (E6(r)) for test example 1.

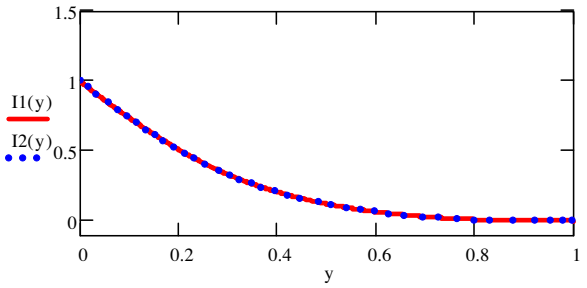

Fig. 7. Distribution of lateral intensities without noise (I1(y)) and with noise (I2(y)) for test example 2.

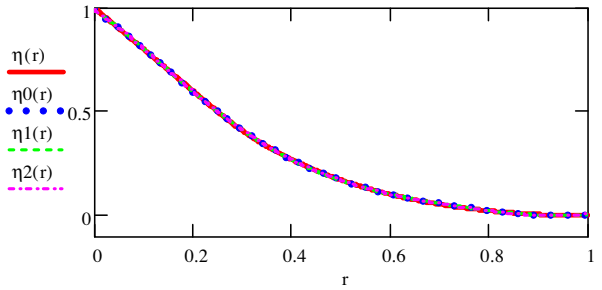

Fig. 8. Reconstructed inverse Abel transforms (emissivity) for test example 2 where profiles are presented as exact profile ($\eta(r)$), approximated profile without noise ($\eta 0(r)$), approximated profile with noise δ_1 ($\eta 1(r)$), and approximated profile with noise δ_2 ($\eta 2(r)$).

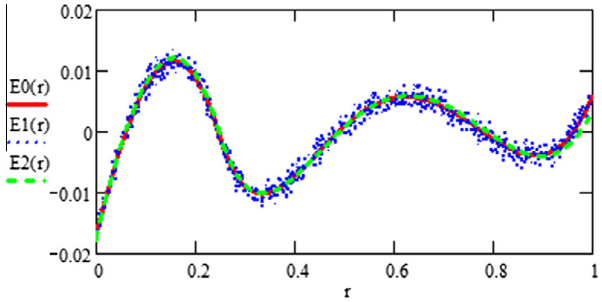

Fig. 9. Comparison of the errors for test example 2, where E0(r) represents error without noise, E1(r) error with noise δ_1, and E2(r) represents error with noise δ_2.

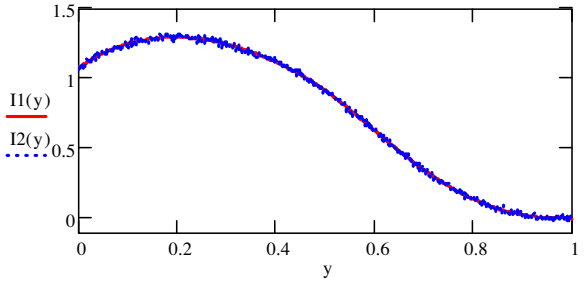

Fig. 10. Distribution of lateral intensities without noise (I1(y)) and with noise (I2(y)) for test example 3.

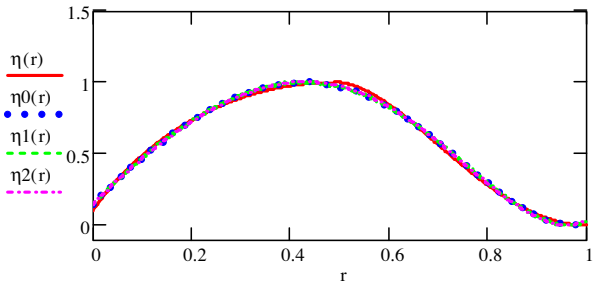

Fig. 11. Reconstructed inverse Abel transforms (emissivity) for test example 3 where profiles are presented as exact profile ($\eta(r)$), approximated profile without noise ($\eta 0(r)$), approximated profile with noise $\delta_1(\eta 1(r))$, and approximated profile with noise δ_2 ($\eta 2(r)$).

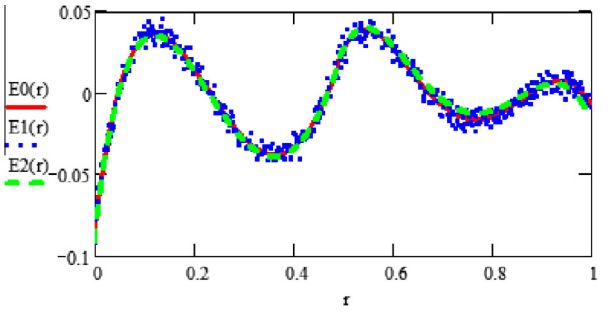

Fig. 12. Comparison of the errors for test example 3, where E0(r) represents error without noise, E1(r) error with noise δ_1, and E2(r) represents error with noise δ_2.

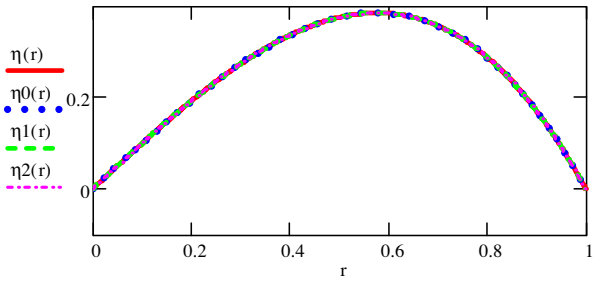

Fig. 13. Reconstructed inverse Abel transforms (emissivity) for test example 4 where profiles are presented as exact profile ($\eta(r)$), approximated profile without noise ($\eta 0(r)$), approximated profile with noise $\delta_1(\eta 1(r))$, and approximated profile with noise δ_2 ($\eta 2(r)$).

For this study, the obtained values of $A^T, \sigma, \mu,$ and $\|\Delta\eta\|_2$ for $N = 1000$, are given as

$$A^T = [0.705 \quad -0.388 \quad -0.277 \quad 0.166 \quad 9.715 \times 10^{-8} \quad -2.236 \times 10^{-7}],$$

$$\sigma = 1.684 \times 10^{-7}, \quad \mu = 0.761, \quad \|\Delta\eta\|_2 = 1.69 \times 10^{-7} \quad \text{and} \quad \delta_2 = 10\%\ \mu_{1000}.$$

From Fig. 2, we observe that given lateral intensity profiles with and without noise almost coincide each other. This demonstrates that the intensity profile can sustain a high level of noise up to $10\%\ \mu_{1000}$. The emission profiles are plotted along with the reconstructed emission profile with and without noise in Fig. 3. Considering the situation when the reconstructed emission profile is influenced by noise, the noise δ_1 is added in the reconstructed emission profile ($\eta 0(r)$) for the purpose. In another case, when given data (intensity profile) is corrupted by noise, we consider the noisy data where noise δ_2 is added to given intensity profile ($I_1(y)$). Fig. 3 clearly shows that the proposed method performs well under the presence of high level of noise in the data. So, it is observed that the reconstructed profiles can sustain high level of noise available in the data. The errors for these cases are plotted in Fig. 4 where we observe that the effect of noise δ_2 is more than the noise δ_1. In Figs. 5 and 6, comparison of the errors for $N = 1000$ (E1(r)), $N = 500$ (E3(r)), and $N = 100$ (E5(r)) for test example 1 are plotted, respectively for parameters $\delta_1$and δ_2.

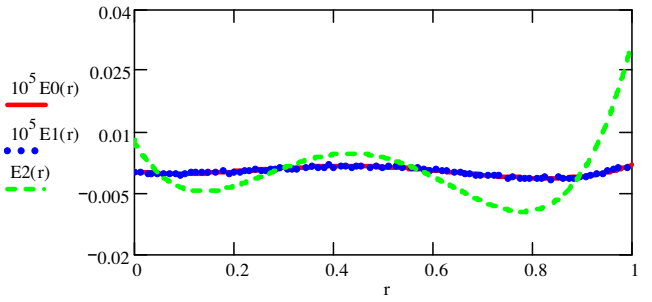

Fig. 14. Comparison of the errors for Test example 4, where E0(r) represents error without noise, E1(r) error with noise δ_1, and E2(r) represents error with noise δ_2.

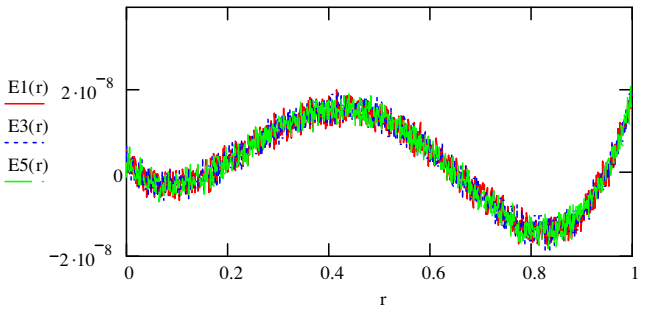

Fig. 15. Comparison of errors with noise δ_1 for $N = 1000$ (E1(r)), $N = 500$ (E3(r)) and $N = 100$ (E5(r)) for test example 4.

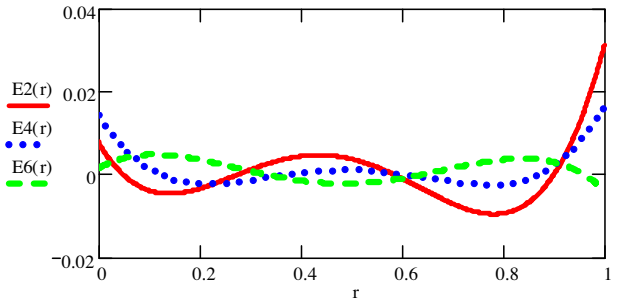

Fig. 16. Comparison of absolute errors with noise δ_2 for $N = 1000$ (E2(r)), $N = 500$ (E4(r)) and $N = 100$ (E6(r)) for test example 4.

Test example 2. Consider the pair [12,19,21,22,28]

$$\eta(r) = \begin{cases} 1 - 2r & \text{if } 0 \leqslant r \leqslant 0.25 \\ 2\left(1 - \sqrt{r}\right)^2 & \text{if } 0.25 < r \leqslant 1 \end{cases}$$

and

$$I_1(y) = \begin{cases} \frac{4\left(\sqrt{1-y}\right)(1+2y)}{3} - \frac{2\left(\sqrt{\frac{1-4y}{4}}\right)(1+8y)}{3} - 4y \ln \frac{1+\sqrt{1-y}}{0.5+\sqrt{\frac{1-4y}{4}}} & \text{if } 0 \leqslant y \leqslant 0.25 \\ \frac{4\left(\sqrt{1-y}\right)(1+2y)}{3} - 4y^2 \ln \frac{1+\sqrt{1-y}}{\sqrt{y}} & \text{if } 0.25 < y \leqslant 1 \end{cases}.$$

For this example, the values of A^T, σ, μ, and $\|\Delta\eta\|_2$ for $N = 1000$, are given as

$$A^T = [0.434 \quad -0.437 \quad 0.147 \quad -0.01 \quad -0.0116.877 \times 10^{-3}],$$

$$\sigma = 2.387 \times 10^{-3}, \quad \mu = 0.25, \quad \|\Delta\eta\|_2 = 2.383 \times 10^{-3} \quad \text{and} \quad \delta_2 = 10\%\ \mu_{1000}.$$

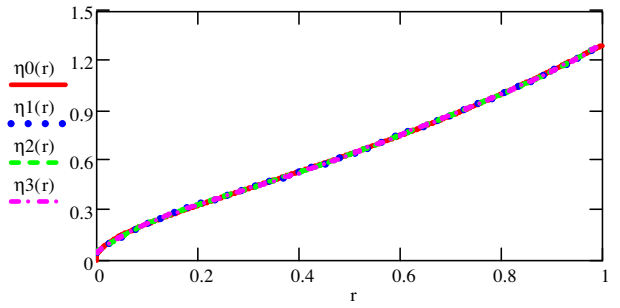

Fig. 17. Reconstructed inverse Abel transforms (emissivity) for test example 5 where profiles are presented as exact profile ($\eta(r)$), approximated profile without noise ($\eta 0(r)$), approximated profile with noise $\delta_1(\eta 1(r))$, and approximated profile with noise δ_2 ($\eta 2(r)$).

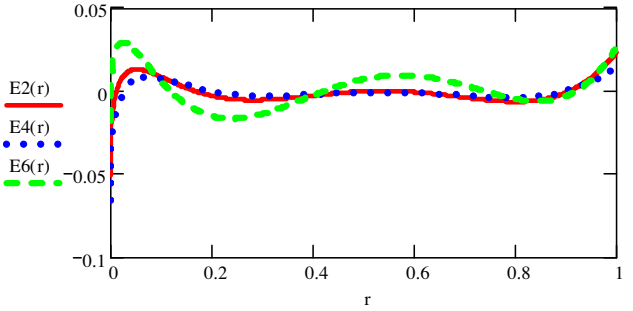

Fig. 18. Comparison of absolute errors with noise δ_2 for $N = 1000$ (E2(r)), $N = 500$ (E4(r)) and $N = 100$ (E6(r)) for test example 4.

Here, we consider the piece wise profile, for which, in general, it is difficult to reconstruct the emission profile accurately. Fig. 8 indicates that the emission profile is reconstructed perfectly even if there is presence of high level of noise in the intensity profiles and reconstructed profiles. And, Fig. 9 represents the comparison of the errors for test example 2, where E0(r) represents error without noise, E1(r) error with noise δ_1, and E2(r) represents error with noise δ_2 .

Test example 3. In this example, we take the pair [22,28],

$$\varepsilon(r) = \begin{cases} 0.1 - 5.51r - 5.25r^3 & \text{if } 0 \leqslant r \leqslant 0.49 \\ -40.74 + 155.56r - 188.89r^2 + 70.07r^3 7 & \text{if } 0.49 < r \leqslant 1 \end{cases},$$

$$I(y) = \begin{cases} 22.68862\sqrt{0.7^2 - y^2} + 217.557y^2\sqrt{0.7^2 - y^2} - 59.49y^4 \ln\left(\frac{1+\sqrt{0.7^2-y^2}}{0.7+\sqrt{0.7^2-y^2}}\right) \\ \quad +155.56y^2 \ln\left(\frac{1+\sqrt{1-y^2}}{0.7+\sqrt{0.7^2-y^2}}\right) + I^*(y) & \text{if } 0 \leqslant y \leqslant 0.49, \\ I^*(y) + 155.56y^2 \ln\left(\frac{1+\sqrt{1-y^2}}{y}\right) & \text{if } 0.49 < y \leqslant 1 \end{cases}$$

where,

$$I^*(y) = -14.811667\sqrt{1-y^2} - 196.30083y^2\sqrt{1-y^2} + 55.5525y^4 \ln\left(\frac{1+\sqrt{1-y^2}}{y}\right).$$

Then, we have, $\eta(r) = \varepsilon(\sqrt{r})$ and $I_1(y) = I(\sqrt{y})$.

The obtained values of $A^T, \sigma, \mu,$ and $\|\Delta\eta\|_2$ for $N = 1000$, are given as:

$$A^T = [0.567 \quad -0.163 \quad -0.393 \quad 0.096 \quad 0.066 \quad 0.015],$$

$$\sigma = 0.018, \quad \mu = 0.752, \quad \|\Delta\eta\|_2 = 0.018 \quad \text{and} \quad \delta_2 = 10\%\ \mu_{1000}.$$

For this case, the emission profile is perfectly reconstructed and plotted in Fig. 11. It is also observed from Fig. 12 that the effect of noise is negligible in this case. The proposed method is validated and we see that there is not much variation in the errors as shown in Fig. 12.

Test example 4. Here, we consider the following example [29]

$$\eta(r) = r - r^3, \quad I_1(y) = \frac{4}{3}y^{3/2} - \frac{32}{35}y^{7/2}.$$

For this example, the values of $A^T, \sigma, \mu,$ and $\|\Delta\eta\|_2$ for $N = 1000$ are given as

$$A^T = [0.235 \quad 0.028 \quad -0.166 \quad -0.028 \quad 5.818 \times 10^{-8} \quad 1.34 \times 10^{-7}],$$

$$\sigma = 1.016 \times 10^{-7}, \quad \mu = 0.33, \quad \|\Delta\eta\|_2 = 1.012 \times 10^{-7} \quad \text{and} \quad \delta_2 = 10\%\ \mu_{1000}.$$

For this pair of test profiles, a different operational matrix Q is calculated to approximate the reconstructed profiles. The emission profile is plotted along with the reconstructed emission profiles with and without noise. We consider the case where the reconstructed profile is influenced by noise, the noise δ_1 is added in the reconstructed emission profile ($\eta 0(r)$). And in another case, we study the performance of the proposed method on the presence of high level of noise in the given data (intensity profile). And, in this case, the noise δ_2 is added to given intensity profile ($I_1(y)$) to test the proposed algorithm. From Fig. 13, one can observe that the effect of noise is not severe even if high level of noise is added in the data. The proposed algorithm performs well in the presence of high level of noise in the data and thus justifies the importance of the proposed algorithm. Fig. 14 shows the error variation and indicates that the presence of noise δ_2 in the data is more than the added noise δ_1. Figs. 15 and 16 demonstrate that the variation of errors under the effect of noises δ_1 and δ_2 are nearly independent with respect to the number of data points.

Test Example 5. We take the following example [25,30],

$$\eta(r) = \frac{e^r erf(\sqrt{r})}{\sqrt{\pi}} \quad \text{and} \quad I_1(y) = e^y - 1.$$

For this example, the values of $A^T, \sigma, \mu,$ and $\|\Delta\eta\|_2$ for $N = 1000$ are given as

$$A^T = [0.829, 0.528, 0.018, 0.023, -7.93 \times 10^{-3}, 7.49 \times 10^{-3}], \quad \sigma = 3.665 \times 10^{-3},$$
$$\mu = 0.719, \quad \|\Delta\eta\|_2 = 3.73 \times 10^{-3} \quad \text{and} \quad \delta_2 = 10\%\ \mu_{1000}$$

Fig. 17 demonstrates the reconstruction ability of the proposed algorithm considering the effect of noise δ_1 ($\eta 1(r)$), noise δ_2 ($\eta 2(r)$) and in absence of noise $\eta 0(r)$, respectively. Similarly, the given emission profile is plotted along with the reconstructed profiles with and without noise. It is observed that the proposed method performs well even in the presence of high level of noise in the data. Fig. 18 demonstrates the variation of the error under the noises δ_1 and δ_2. Table 1 illustrates the comparison of the RMS error under the effect of noise and without noise. Considering the worst case scenario where, noise ($\delta_2 = 10\%\ \mu$) has been added for analysis purpose and corresponding RMS errors are obtained. Here, number of data points is considered as $N = 30$. Even in the presence of high level of noise in the data, RMS error is found appreciable than others.

Table 1
Comparison of RMS Error "σ" (without and with noise) for different test examples for $N = 30$, $\delta_2 = 10\%\ \mu$, and $m = 5$.

Test examples	RMS error (without noise)		RMS error (with noise)	
	Proposed method $N = 30$	Other methods $N = 30$	Proposed method $N = 30$, $\delta_2 = 10\%\ \mu$	Other methods $N = 30$
Test example 1	2.305×10^{-7}	0 [28]	1.652×10^{-3}	0.0121 [28]
Test example 2	2.441×10^{-3}	0.0014 [28]	4.294×10^{-3}	0.0101 [28]
Test Example 3	0.0181	0.0056 [28]	0.0197	0.0199 [28]
Test example 4	1.226×10^{-6}	3.994×10^{-7} [30]	2.437×10^{-3}	2.714×10^{-3} [30]
Test example 5	3.786×10^{-3}	3.077×10^{-3} [30]	5.955×10^{-3}	4.314×10^{-3} [30]

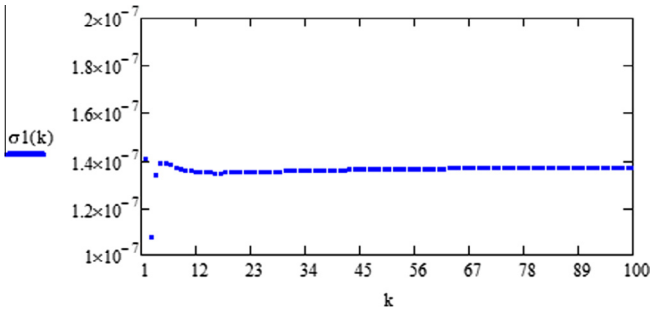

Fig. 19. Variation of the RMS error with respect to number of data points taken up to 100 for test example 1.

Similarly, for the piece wise test profiles (test examples 2 and 3), one can observe that the reconstruction of the emission profiles (Figs. 8 and 11) with and without noise has better accuracy throughout the support of the profiles.

The variation of the RMS error ($\sigma 1(k)$) with the number of data points (k) can be seen in the following Fig. 19.

From the above Fig. 19, one can observe that the RMS error is not varying much when the data point $N > 10$. Also, there is very less variation (10^{-7}) when $N < 10$. Similarly for the piecewise profile (test example 2), there is no variation in RMS error when $N > 15$ and varies slightly when $N < 15$. The RMS error variation ($\sigma 2(k)$) plot is given in Fig. 20 for test example 2.

In addition, the errors (with and without noise) are comparatively good in the support of the profiles, which specifies one of the advantage of the proposed algorithm over the other algorithms available in the literature. The proposed approach has the following additional advantages over the previous algorithms: only small size of the operational matrix is required to provide the results at high accuracy and also provides good reconstruction for the different types of profiles. The method is quite stable even if the high level of noise is added in the intensity profiles and thus the errors obtained at boundary, known as termination error, are also appreciable.

Remark: Piessens and Verbaeten [13] used the Chebyshev polynomials to approximate the solution of the Abel integral equation. The philosophy of the method is to approximate the unknown function appearing in the integral equation in the terms of the generalized hypergeometric functions. For comparison purpose here, we consider example 2 of [13] as follows:

$$I_1(y) = \frac{\sqrt{\pi}(1-y)^{-1/2}\, e^{\left[1.21\left(1-\frac{1}{1-y}\right)\right]}}{1.1}; \quad \eta(r) = (1-r)^{-3/2}\, e^{\left[1.21\left(1-\frac{1}{1-r}\right)\right]}. \tag{20}$$

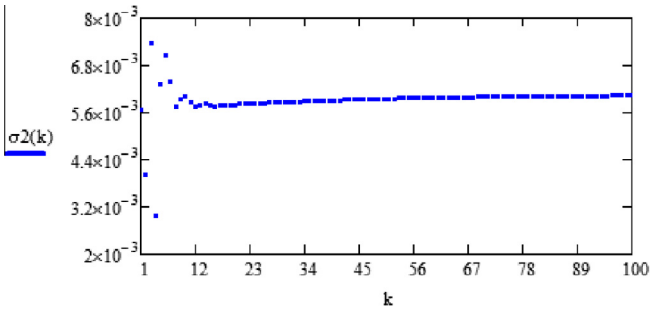

Fig. 20. Variation of the RMS error with respect to number of data points taken up to 100 for example 2.

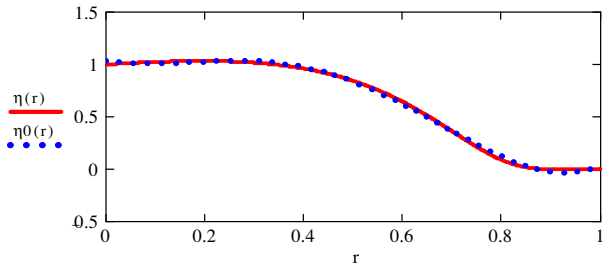

Fig. 21. Reconstructed inverse Abel transforms (emissivity) for pair given in Eq. (20) where profiles are presented as exact profile ($\eta(r)$), approximated profile without noise ($\eta 0(r)$).

Table 2
Comparison of the errors for the pair (Eq. (20)) with present method and method [13].

Value (r)	Method in [13] for $m = 9$	Proposed method for $m = 5$ (without noise)	Proposed method for $m = 5$ (with $\delta_2 = 10\%\ \mu$)	Proposed method for $m = 9$ (without noise)
0.0	0.14×10^{-1}	−0.036	−0.038	-5.837×10^{-3}
0.1	0.65×10^{-2}	0.016	0.016	2.803×10^{-4}
0.2	-0.82×10^{-2}	3.566×10^{-3}	4.022×10^{-3}	-1.752×10^{-3}
0.3	-0.12×10^{-1}	−0.016	−0.015	2.382×10^{-3}
0.4	-0.81×10^{-3}	−0.013	−0.012	3.169×10^{-4}
0.5	0.52×10^{-3}	0.01	0.01	-3.417×10^{-3}
0.6	0.35×10^{-2}	0.024	0.024	1.762×10^{-3}
0.7	0.45×10^{-2}	-1.901×10^{-3}	-2.285×10^{-3}	3.407×10^{-3}
0.8	0.15×10^{-2}	−0.034	−0.034	-6.854×10^{-3}
0.9	-0.32×10^{-2}	0.027	0.022	7.732×10^{-3}

The proposed method has been used to approximate the emission profile for the same pair of profiles given in Eq. (20). The reconstructed emissivity profile along with the exact profile is plotted in (Fig. 21), whereas Table 2 shows the obtained errors at the different point using proposed technique.

In Table 2, for comparison purpose, we consider the different values of m as 5 and 9 for the proposed algorithm and $m = 9$ for algorithm presented in [13]. We have also tested the proposed algorithm under the effect of noise ($\delta_2 = 10\%\ \mu$). And it is observed that the obtained results from the proposed method are found comparable with existing method [13] for $m = 5$ and found better for $m = 9$.

5. Conclusions

We constructed the modified Chebyshev operational matrix of integration to present a stable algorithm for Abel's inversion. The proposed algorithm is applied to obtain Abel's inversion for different test profiles in nature. Applicability of the proposed method is illustrated through different test examples and stability of the algorithm is analyzed with respect to the noise added in the data. Comparatively good accuracy is obtained even for the small sample intervals and high noise levels in the data. The proposed approach found comparatively better over other methods as only small size operational matrix is required to obtain the inversion at good accuracy. It also provides good reconstruction for the different types of profiles. The method is found quite stable even if there is high level of noise present in the intensity profiles and the errors obtained at the boundary are also comparable.

Acknowledgement

The authors are grateful to the reviewers for their valuable comments which have been incorporated to improve the quality of the manuscript. Funding support from Science and Engineering Research Board of Department of Science & Technology, Government of India under fast track scheme SR/FTP/MS-016/2012 is also acknowledged.

References

[1] N.H. Abel, Resolution d'un probleme de mechanique, J. Reine Angew. Math. 1 (1826) 153–157.
[2] S.B. Healy, J. Haase, O. Lesne, Abel transform inversion of radio occultation measurements made with a receiver inside the Earth's atmosphere, Ann. Geophys. 20 (2002) 1253–1256.
[3] S.C. Solomon, P.B. Hays, V.J. Abreu, Tomographic inversion of satellite photometry, Appl. Opt. 23 (1984) 3409–3414.
[4] E.L. Kosarev, Applications of integral equations of the first kind in experiment physics, Comput. Phys. Commun. 20 (1980) 69–75.
[5] U. Buck, Inversion of molecular scattering data, Rev. Mod. Phys. 46 (1974) 369–389.
[6] C.J. Tallents, M.D.J. Burgess, B. Luther-Davies, The determination of electron density profiles from refraction measurements obtained using holographic interferometry, Opt. Commun. 4 (1983) 384–387.
[7] M. Deutsch, A. Notea, D. Pal, Inversion of Abel's integral equation and its application to NDT by X-ray radiography, NDT Int. 23 (1) (1990).
[8] D.N. Ghosh Roy, Radon inversion of plasma emission, Phys. Lett. A 96 (9) (1983) 463–466.
[9] M.J. Buie, J.T.P. Pender, J.P. Holloway, T. Vincent, P.L.G. Ventzek, M.L. Brake, Abel's inversion applied to experimental spectroscopic data with off axispeaks, J. Quantum Spectrosc. Radiat. Transfer 55 (2) (1996) 231–243.
[10] F.G. Tricomi, Integral Equations, Inter science, New York, 1975.
[11] G.N. Minerbo, M.E. Levy, Inversion of Abel's integral equation by means of orthogonal polynomials, SIAM J. Numer. Anal. 6 (1969) 598–616.
[12] M. Deutsch, I. Beniaminy, Derivative-free inversion of Abel's integral equation, Appl. Phys. Lett. 41 (1982) 27–28.
[13] R. Piessens, P. Verbaeten, Numerical Solution of the Abel integral equation, BIT Numerical Mathematics 13 (1973) 451–457.
[14] R.S. Anderssen, Stable procedures for the inversion of Abel's equation, J. Inst. Math. Appl. 17 (1976) 329–342.
[15] J.P. Lanquart, Error attenuation in Abel inversion, J. Comput. Phys. 47 (1982) 434–443.
[16] R. Grenflo, Computation of rough solutions of Abel integral equation, in: H.W. Engel, C.W. Groetsch (Eds.), Inverse III—posed problems, Academic Press, New York, 1987, pp. 195–210.
[17] M. Sato, Inversion of the Abel integral equation by use of simple interpolation formulas, Contrib. Plasma Phys. 25 (1985) 573–577.
[18] M. Deutsch, Abel inversion with a simple analytic representation for experimental data, Appl. Phys. Lett. 42 (1983) 237–239.
[19] I. Beniaminy, M. Deutsch, M. Abel, Stable high accuracy program for the inversion of Abel's integral equation, Comput. Phys. Commun. 27 (1982) 415–422.
[20] D.A. Murio, D.G. Hinestroza, C.E. Mejia, New stable numerical inversion of Abel's integral equation, Comput. Math. Appl. 23 (11) (1992) 3–11.
[21] Y.T. Cho, S.-J. Na, Application of Abel inversion in real-time calculations for circularly and elliptically symmetric radiation sources, Meas. Sci. Technol. 16 (2005) 878.
[22] C.Y. George Chan, G.M. Hieftje, Estimation of confidence intervals for radial emissivity and optimization of data treatment techniques in Abel inversion, Spectrochim. Acta Part B 61 (2006) 31–41.
[23] S.A. Yousefi, Numerical solution of Abel's integral equation by using Legendre wavelets, Appl. Math. Comput. 175 (2006) 574–580.
[24] R.K. Pandey, O.P. Singh, V.K. Singh, Efficient algorithms to solve singular integral equations of Abel type, Comput. Math. Appl. 57 (4) (2009) 664–676.
[25] O.P. Singh, V.K. Singh, R.K. Pandey, New stable numerical inversion of Abel's integral equation using almost Bernstein operational matrix, J. Quant. Spectrosc. Radiat. Transfer 111 (2010) 245–252.
[26] S. Ma, H. Gao, L. Wu, G. Zhang, Abel inversion using Legendre polynomials approximations, J. Quant. Spectrosc. Radiat. Transfer 109 (2008) 1745–1757.
[27] S. Ma, H. Gao, G. Zhang, L. Wu, Abel inversion using Legendre wavelets expansion, J. Quant. Spectrosc. Radiat. Transfer 107 (1) (2007) 61–71.
[28] Xian-Fang Li, L. Huang, Y. Huang, A new Abel inversion by means of the integrals of an input functions with noise, J. Phys. A: Math. Theor. 40 (2007) 347–360.
[29] L. Huang, Y. Huang, Xian-Fang Li, Approximate solution of Abel integral equation, Comput. Math. Appl. 56 (2008) 1748–1757.
[30] V.K. Singh, R.K. Pandey, O.P. Singh, New stable numerical solutions of singular integral equations of Abel type by using normalized Bernstein polynomials, Appl. Math. Sci. 3 (2008) 441–455.